

# Chrono CDI: Coherent diffractive imaging of time-evolving samples

A. Ulvestad,<sup>1</sup> A. Tripathi,<sup>2</sup> S. O. Hruszkewycz,<sup>1</sup> W. Cha,<sup>1</sup> S. M. Wild,<sup>2</sup> G. B. Stephenson,<sup>1</sup> and P. H. Fuoss<sup>1</sup>

<sup>1</sup>Materials Science Division, Argonne National Laboratory, Lemont, IL 60439, USA

<sup>2</sup>Mathematics and Computer Science Division, Argonne National Laboratory, Lemont, IL 60439, USA

Bragg coherent x-ray diffractive imaging is a powerful technique for investigating dynamic nanoscale processes in nanoparticles immersed in reactive, realistic environments. Its temporal resolution is limited, however, by the oversampling requirements of 3D phase retrieval. Here we show that incorporating the entire measurement time series, which is typically a continuous physical process, into phase retrieval allows the oversampling requirement at each time step to be reduced leading to a subsequent improvement in the temporal resolution by a factor of 2-20 times. The increased time resolution will allow imaging of faster dynamics and of radiation-dose-sensitive samples. This approach, which we call “chrono CDI,” may find use in improving time resolution in other imaging techniques.

## I. INTRODUCTION

Understanding nanoscale processes is key to improving the performance of advanced technologies, such as batteries, catalysts, and fuel cells. However, many processes occur inside devices at short length and time scales in reactive environments and represent a significant imaging challenge. Bragg coherent diffractive imaging (BCDI) has emerged as a powerful technique for revealing 3D nanoscale structural information.<sup>1,2</sup> With current BCDI methods, 3D image reconstructions of nanoscale crystals have been used to identify and track dislocations,<sup>3,4</sup> image cathode lattice strain during battery operation,<sup>5,6</sup> indicate the presence of surface adsorbates,<sup>7,8</sup> and reveal twin domains.<sup>9,10</sup> The temporal resolution of current BCDI experiments, however, is limited by the oversampling requirements for current phase retrieval algorithms. The insight developed in this work is that, for most physical processes, structural evolution is a continuous process that introduces structural redundancy when measured as a time series. Here, we exploit this redundancy to allow for reduced oversampling (less than the conventionally required factor of 2), thereby improving the measurement rate. In principle, this method can also be used to increase the spatial resolution.

Our new approach, which we call “chrono CDI,” improves the temporal resolution of BCDI by reducing the oversampling requirement along one dimension ( $q_z$ ) at a given time step without significantly compromising image fidelity. To enable this capability, we designed a reconstruction algorithm that simultaneously reconstructs all time states in a series of Bragg rocking curves by utilizing constraints from neighboring time steps. In this work, the initial and final states are assumed to be known in real space. In practice, this situation is achieved provided both states are measured with the required oversampling (OS). The time frame over which the sample is assumed to be static (the measurement time of an individual rocking curve) is reduced in chrono CDI, providing access to faster dynamics in 3D crystals. In addition, this approach can be used to limit the radiation dose in radiation-sensitive samples and/or increase the spatial resolution by allowing for reduced sampling in  $q_x$  and  $q_y$ .

Figure 1a shows a schematic of a Bragg rocking curve. The rocking curve entails rotating the sample with respect

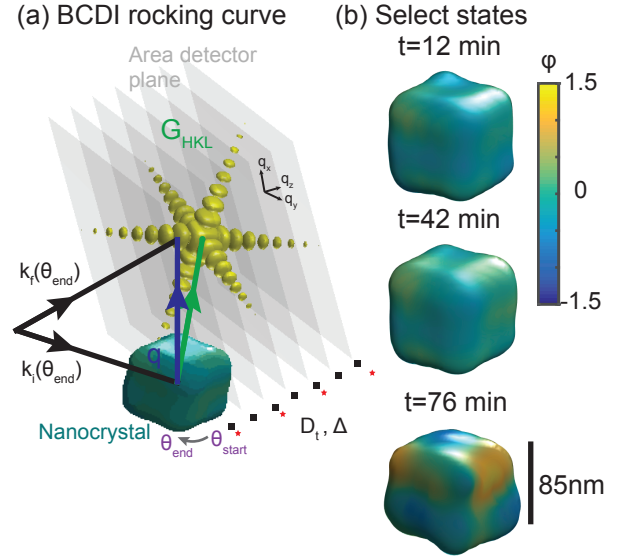


FIG. 1. Bragg CDI experiment of a single time-evolving nanocrystal: (a) Schematic of a Bragg rocking curve. The rocking curve involves rotating the sample with respect to the incident x-rays  $\mathbf{k}_i$ . Here,  $\mathbf{k}_f$  represents the scattered x-rays,  $\mathbf{q}$  the particular scattering vector, and  $\mathbf{G}_{hkl}$  the particular Bragg peak. The rocking curve sweeps the 2D area detector through the 3D volume in the  $q_z$  direction. Conventionally, all 2D measurements shown by black boxes are required; in order to improve the time resolution, only some 2D measurements (red stars) could be taken.  $D_t$  denotes the full 3D diffraction measurement and  $\Delta$  the time required to make the full measurement. (b) Select time states from the time sequence that was reconstructed from experimental BCDI data measured with greater than the required oversampling. The isosurface is drawn at a constant Bragg electron density and represents the shape of the 85 nm Pd nanocube. The isosurface color is the imaginary part of the image, the phase  $\phi$ , which is proportional to the  $u_{111}$  displacement field.

to the incident x-ray beam  $\mathbf{k}_i$ . The sample rotation, labeled schematically by  $\theta_{\text{start}}$  and  $\theta_{\text{end}}$ , displaces the scattering vector  $\mathbf{q} = \mathbf{k}_f - \mathbf{k}_i$  from the reciprocal-space lattice point  $\mathbf{G}_{hkl}$ , the Bragg reflection condition for the HKL lattice planes, so that the 3D intensity distribution (yellow isosurface) can be appropriately sampled and the structure of the nanocrystal (green cube) can be reconstructed. The series of 2D measurements (grey planes in Fig. 1a) are stacked to form a 3D dataset  $D_t$ ,

where  $t$  represents a time index in a series of sequential rocking curve measurements. The total time for the measurement is  $\Delta$ . Current phase retrieval algorithms require an oversampling of at least 2 of the diffraction pattern in all three dimensions. We refer to an oversampling of 2 as the required oversampling. In addition, the nanocrystal must be approximately static over the measurement time  $\Delta$  while  $D_t$  is collected, which limits the dynamic timescale that can be observed.<sup>11,12</sup>

Figure 1b shows three select time states from a time series during which a single crystal palladium nanocube (85 nm side length) is exposed to hydrogen gas. Experimental details are given in a recent publication.<sup>13</sup> The absolute value of the image (shown as an isosurface) corresponds to the Bragg-diffracting electron density,<sup>9</sup> while the phase,  $\phi$ , of the image (color projected onto the isosurface) is proportional to a component of the vector displacement field  $\mathbf{u}$  via  $\phi = \mathbf{u} \cdot \mathbf{Q}$ .<sup>1,14,15</sup> In this case, the Pd (111) Bragg peak was measured and  $\phi \sim u_{111}$ . In the Pd nanocube, hydrogen intercalation initially causes displacement field changes ( $t = 42$  minutes) before morphological changes occur ( $t = 76$  minutes) due to the hydriding phase transformation.<sup>16,17</sup> The time evolution of the nanocube structure shown in Fig. 1b was determined from BCDI experiments performed with an oversampling of 3 in  $q_z$  at Sector 34-ID-C of the Advanced Photon Source at Argonne National Laboratory (see Experimental Details in Supplemental Material and Ulvestad, et al.<sup>13</sup>). Each complete measurement took approximately 2 minutes ( $\Delta$  in Fig. 1).

## II. ALGORITHMIC APPROACH

To incorporate the redundancy in correlated time series such as those in Fig. 1, we modify conventional BCDI phase retrieval algorithms. The function minimized by the error reduction phase retrieval algorithms is the modulus error,  $\varepsilon_{\mathcal{M}}^2$ , which measures the agreement between the reconstruction's Fourier moduli and the measured moduli,

$$\varepsilon_{\mathcal{M}}^2(\rho, D) = \sum_{\mathbf{q}} \left| |\tilde{\rho}| - \sqrt{D} \right|^2,$$

where  $\rho$  is the 3D reconstructed object (in real space),  $D$  is the 3D far-field intensity measurement,  $\mathbf{q}$  is the reciprocal-space coordinate,  $\tilde{\rho} = \mathcal{F}[\rho]$ , and  $\mathcal{F}$  is the Fourier transform. Different choices of the function to be minimized lead to different phase retrieval algorithms.<sup>18</sup> In chrono CDI, we include a term that depends on reconstructions at other time states,

$$\sum_t \left[ \varepsilon_{\mathcal{M}}^2(\rho_t, D_t) + \sum_{t' \neq t} w(t, t') \mu(\rho_t, \rho_{t'}) \right]. \quad (1)$$

In this expression,  $t$  indexes the time states,  $w(t, t')$  is the weight,  $t \neq t'$ , and  $\mu(\rho_t, \rho_{t'})$  is the miscorrelation term. In this paper, we consider nearest-neighbor correlations in time, a scalar weight parameter  $w \geq 0$ , and a functional form for

the miscorrelation of

$$\mu(\rho_t, \rho_{t'}) = \sum_{\mathbf{r}} |\rho_t - \rho_{t-1}|^2 + \sum_{\mathbf{r}} |\rho_t - \rho_{t+1}|^2.$$

The  $t$ th term of the objective in Eq. (1) then becomes

$$\varepsilon_{\mathcal{M}}^2(\rho_t, D_t) + w \left( \sum_{\mathbf{r}} |\rho_t - \rho_{t-1}|^2 + \sum_{\mathbf{r}} |\rho_t - \rho_{t+1}|^2 \right). \quad (2)$$

Although other forms are possible, this form has the advantage of being computationally inexpensive. The iterative algorithm is derived by minimizing Eq. (2) summed over  $t$  (for details, see the Supplemental Material and refs.<sup>18,19</sup>).

## III. NUMERICAL RESULTS

To evaluate the algorithm's performance, we carry out iterative phase retrieval on noise-free, simulated data as well as on measured experimental data with different amounts of oversampling.

### A. Simulated Data with Required Oversampling

In this case, the simulated data  $D_t^{\text{sim}}$  is generated by 3D Fourier transforms of each complex valued Pd nanocube reconstruction in the time series after zero padding to meet the oversampling (OS) requirements of phase retrieval.<sup>20</sup> We refer to an oversampling of 2 as the required oversampling (Req. O.S.). In practice, this means the cube size was half of the array size in all three dimensions. The time sequence considered consists of  $t = 0, 12, 18, 26, 34, 42, 50, 58, 66$ , and 76 minutes. This time sequence is approximately equally spaced and, as shown in Fig. 2, has varying amounts of nearest-neighbor correlation, with an average nearest-neighbor correlation coefficient of 61%. The correlation coefficient  $c(t, t') \in [-1, 1]$  is defined between two 3D displacement fields at time states  $t$  and  $t'$  by

$$\frac{\sum_{\mathbf{r}} [u_{111}(\mathbf{r}, t) - \bar{u}_{111}(\mathbf{r}, t)] [u_{111}(\mathbf{r}, t') - \bar{u}_{111}(\mathbf{r}, t')]}{\sqrt{\sum_{\mathbf{r}} [u_{111}(\mathbf{r}, t) - \bar{u}_{111}(\mathbf{r}, t)]^2} \sqrt{\sum_{\mathbf{r}} [u_{111}(\mathbf{r}, t') - \bar{u}_{111}(\mathbf{r}, t')]^2}}$$

where  $u_{111}$  is the displacement field projection and  $\bar{u}_{111}$  is the average displacement field over the particle.

Figure 3a shows the correlation coefficient matrix for the chosen time sequence. Figure 2 is a plot of the super-diagonal matrix values. The chosen time sequence is a good balance between having smooth evolution between nearest neighbors and having a large change over the whole time sequence (both the displacement and the amplitude change significantly). The first numerical test of chrono CDI reconstructs the sequence  $\rho_t$  from the sequence of  $D_t^{\text{sim}}$  with the required oversampling.

The algorithm uses with random initial starts and alternates between the error reduction (ER) and the hybrid input-output (HIO) algorithms using a feedback parameter of  $\beta = 0.7$ .<sup>21</sup>

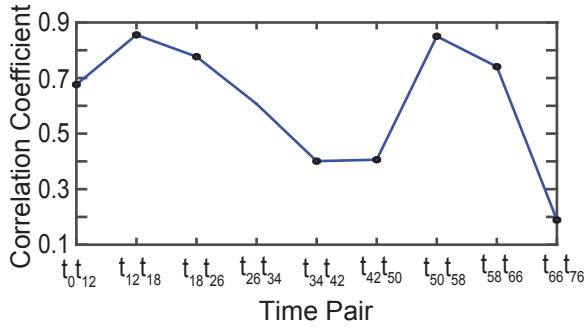


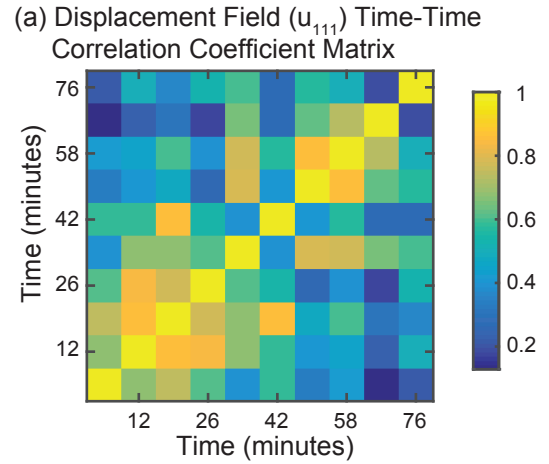
FIG. 2. Nearest-neighbor correlation coefficient of  $u_{111}(\mathbf{r})$  for all pairs in the chosen time sequence. The average nearest-neighbor correlation coefficient is 61%.

the support is fixed to the size of the object and is not evolved during the iterative process. At iteration numbers  $N = 100n$ , for  $n = 1, 2, \dots, 18$ , the algorithm tests whether all reconstructions are correctly oriented with respect to the known initial ( $t = 0$  minutes) and final ( $t = 76$  minutes) states by testing whether they are conjugated and reflected (“twin”) solutions.<sup>21</sup> Although reconstructing the “twin” image does not affect  $\varepsilon_{\mathcal{M}}^2$ , it will negatively impact  $\mu$ , resulting in an artificially high total objective. One constraint used in the present work is that the  $\rho_t$  of the initial and final states are known in real and diffraction space. This constraint can be achieved by measuring diffraction datasets at the required oversampling before the experimental dynamics start and after no significant changes are seen in the diffraction data.

Figure 3b shows the errors  $\varepsilon_{\mathcal{M}}^2(\rho_t, D_t^{\text{sim}})$  and  $\mu(\rho_t, \rho_{t'})$ , averaged over all reconstructed time states and over 10 random starts, as a function of the scalar weight  $w$ . Both errors are normalized by the total intensity in the image. Figure ?? in the Supplemental Material shows the modulus error  $\varepsilon_{\mathcal{M}}^2$  as a function of iteration number for two scalar weight values. The initial and final states ( $t = 0$  and  $t = 76$  minutes, respectively) are known in real space. When  $w = 0$ , the modulus error is the lowest, and the miscorrelation term is the largest. These results are expected because the data is noise-free and oversampled at the required oversampling such that a unique solution is fully determined for each  $D_t^{\text{sim}}$ . The weight  $w = 0$  corresponds to the case when no correlations are taken into account. As  $w$  increases,  $\mu(\rho_t, \rho_{t'})$  decreases, and  $\varepsilon_{\mathcal{M}}^2$  increases for the solution set  $\{\rho_t\}$  because their relative contributions to the total objective change. With data sampled at the required oversampling, including information from neighboring time steps in a time series will not improve each individual reconstruction because the complete 3D structural description of the sample at each time is uniquely encoded in the 3D coherent intensity pattern.

### B. Simulated Data with Reduced Oversampling

We now explore how the additional redundancy from the time series can compensate for reduced oversampling during the rocking curve (e.g. oversampling at less than a factor of 2)



(b) Normalized Average Errors for Perfect Data

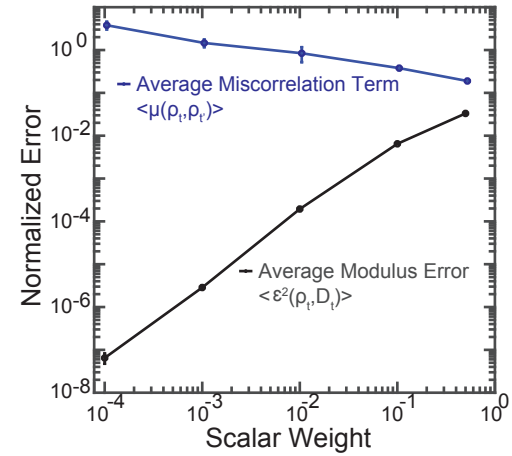


FIG. 3. (a) Time correlation in the [111] displacement field projection,  $u_{111}(\mathbf{r})$ , during the reconstructed time sequence. (b), Average (over all time states and random starts) modulus error  $\varepsilon_{\mathcal{M}}^2(\rho_t, D_t^{\text{sim}})$  (black) and average (over all time states and random starts) miscorrelation term  $\mu(\rho_t, \rho_{t'})$  (blue) normalized by the total intensity in the image as a function of the scalar weight. Error bars represent the standard deviation of the average over all time states obtained from 10 different random starts.

at a given time step by reconstructing the time series  $D_t^{\text{sim}}$  discussed previously but with different degrees of reduced sampling in  $q_z$ . To start, every third 2D diffraction measurement of the original 84 2D diffraction measurements was selected to form  $D_t^{\text{sim}}$  for all times except the initial and final time. This leads to data that has 1/3 of the required oversampling. If such a time series were measured experimentally, the measurement time would be reduced by a factor of 3. In assessing algorithm performance, the modulus error was calculated by comparing the far-field exit wave of the reconstructions with the data sampled at the required oversampling. As before, the initial and final states are known, the support is known, and alternating ER/HIO is used as described previously.

Figure 4a shows the average (over all time states and random starts) modulus error as a function of the scalar weight  $w$  for varying amounts of oversampling. The average normal-

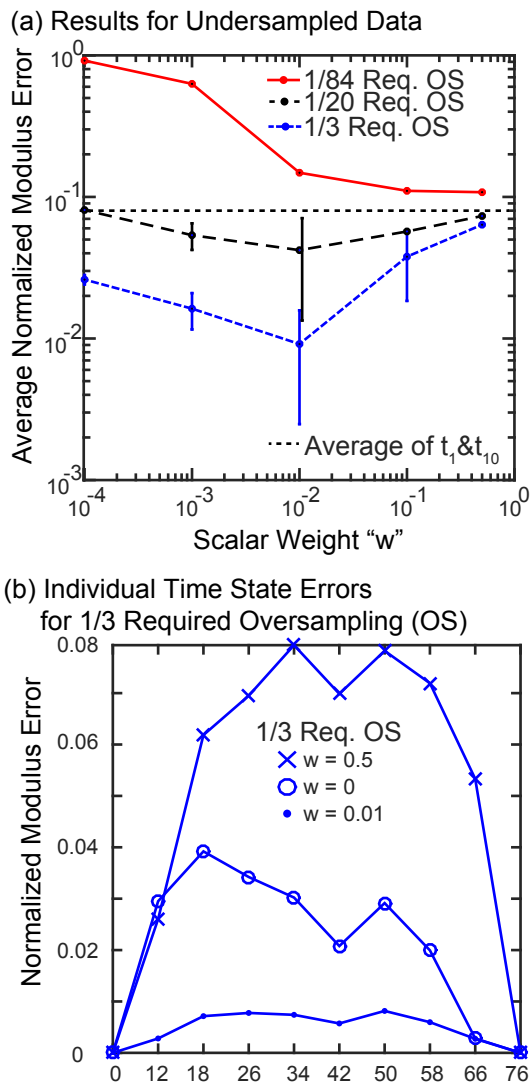


FIG. 4. Results for reduced oversampling (OS). (a) The average (over all time states and random starts) normalized modulus error as a function of the scalar weight  $w$  for 1/3 (blue), 1/20 (black), and 1/84 (red) of the required oversampling.  $w = 0$  (not shown) produces the same average normalized modulus error values as  $w = 10^{-4}$ . The modulus error reported here is computed with respect to the data with the required oversampling. Error bars represent the standard deviation of the different average (over all time states) values obtained from 10 different random starts. Error bar for  $w = 0.01$  and 1/20th (black) of the required oversampling is offset for clarity. The black dashed horizontal line shows the normalized average modulus error using the average of the initial and final time states for every time state in the sequence. (b) The individual time state errors for 1/3 (blue) required oversampling for a particular random start for  $w = 0$  (open circle),  $w = 0.01$  (points), and  $w = 0.5$  (x).

ized modulus error does not change from  $w = 0$  to  $w = 10^{-4}$ . Unlike the results using the required oversampling (shown in Fig. 3b) where the lowest modulus error occurs for  $w = 0$  (no time correlation), in the cases where  $q_z$  has been sampled at 1/3 (blue) and 1/20 (black) of the required oversampling, a minimum in the modulus error is observed at a value

of  $w = 0.01$ . This modulus error is computed with respect to the datasets that are sampled at the required oversampling, and thus the reconstructions at these minima are the “best” solutions. When only 1/84 (red) of the required oversampling is used (i.e., a single slice from the rocking curve), the modulus error decreases with increasing  $w$  and approaches a constant value, which is near the normalized average modulus error when all the reconstructed time states are set to the average of the initial and final state (black dashed horizontal line). In this case, simply using an average of the initial and final states outperforms the reconstruction algorithm, indicating that there are insufficient reciprocal space constraints and that the oversampling in  $q_z$  is too low.

On average  $w = 0.01$  improves the reconstructed time sequence relative to  $w = 0$ , which takes no time correlation into account, for up to 1/20 of the required oversampling. However, it is not clear from the plot of the average whether all time states are being improved equally. Figure 4b shows the normalized modulus error at each time state for  $w = 0, 0.01, 0.5$  at 1/3 of the required oversampling for a particular random start. The states nearest to the known states ( $t = 0$  and  $t = 76$  minutes) have lower modulus errors, as expected. By comparing  $w = 0$  with  $w = 0.01$ , we see that the improvement occurs in all the intermediate states except the state at  $t = 66$  minutes, which remains essentially unchanged. These results demonstrate that the algorithm improves all reconstructions, even those least correlated with their neighbors (see Fig. 2 for a plot of the nearest neighbor correlation). The benefits of chrono CDI are clear when the required oversampling is reduced by up to a factor of approximately 1/20. In these cases, enforcing a degree of nearest-time-step, real-space correlation provides an additional constraint that improves the reconstruction at all intermediate times relative to what can be achieved using conventional phase retrieval.

### C. Experimental Data

We now demonstrate chrono CDI on experimental rocking curve data. To simulate varying degrees of reduced oversampling, a subset of the original 2D measurements was selected from the experimental datasets. Figure 5 shows example 2D experimental diffraction measurements from the Pd (111) Bragg rocking curve; see Ulvestad, et al.<sup>13</sup> for more details. An oversampling of approximately 3 in  $q_z$  was used during the original measurement. The reconstruction algorithm is the same as described previously except that the support is not known a priori. Instead, an initial box half the array size in each dimension is used, and the support is updated with the shrinkwrap algorithm<sup>14,22</sup> using a Gaussian function with a threshold of 0.01 and standard deviation of 1.

Figure 6 shows chrono CDI reconstructions for two representative time states of experimental diffraction data from Pd nanocubes undergoing structural transformations when exposed to hydrogen gas. As before, different amounts of oversampling were investigated. The isosurfaces shown correspond to the reconstructed Bragg electron density, while the color map corresponds to the image phase  $\phi$ , which is pro-

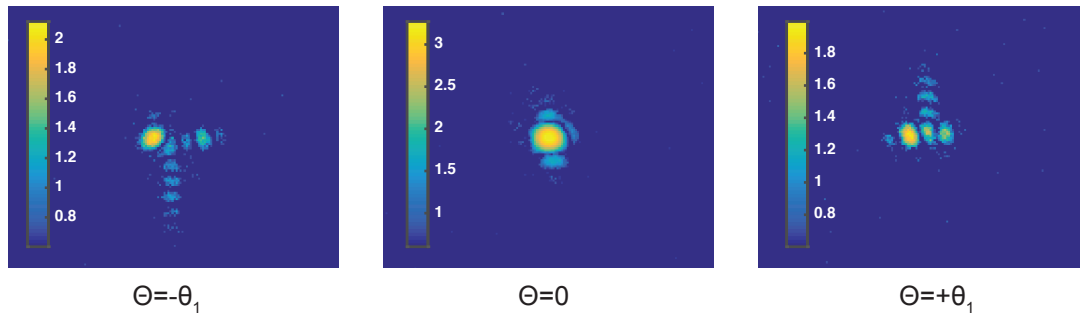
Measured 2D diffraction cross sections,  $t=12$  min

FIG. 5. Three cross sections of the real data from  $t = 12$  minutes used to test the chrono CDI algorithm. The color bar is the  $\log_{10}$  of the number of photons. The data is oversampled by a factor of 3 in  $q_z$  and has both noise and a finite scattering extent. These measured datasets, after background subtraction (1–2 photons) and the removal of a number of 2D slices, are used to test the chrono CDI algorithm. Please see Ulvestad, et al.<sup>13</sup> for further details.

Reconstructions of Real Data with 1/2 Req. OS

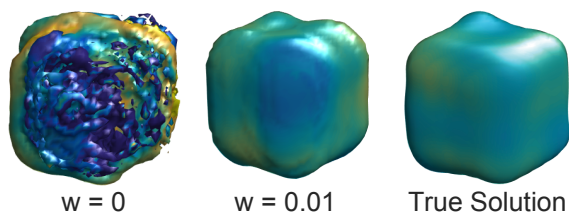
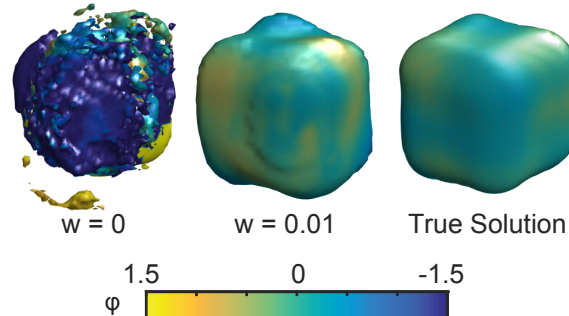
a)  $t=12$  minb)  $t=42$  min

FIG. 6. Reconstructions of experimental measurement data with reduced oversampling. The real part of the image (shown as an isosurface) corresponds to the reconstructed Bragg electron density, while the complex part of the image (colormap projected onto the isosurface) corresponds to the reconstructed displacement field projection. (a) The  $t = 12$  minutes reconstructions for 1/2 of the required oversampling for  $w = 0$  and  $w = 0.01$ , and the true solution. (b) The same as (a) but for the  $t = 42$  minutes reconstruction.

portional to the  $u_{111}$  displacement field. Figure 6a shows reconstructions when 1/2 of the required oversampling in  $q_z$  is used. Every third slice of the original data (oversampled at a factor of 3 in  $q_z$ ) was used to generate data. This corresponds to an oversampling of 1, which is 1/2 the required oversampling of 2. The reconstruction for  $w = 0.01$  is much improved compared with  $w = 0$  and is similar in morphology and lat-

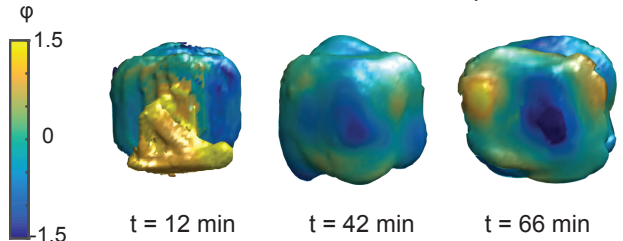
Reconstructions of Real Data with 3/10 Req. OS,  $w=0.01$ 

FIG. 7. Reconstructions of real measurement data with 3/10 of the required oversampling and  $w = 0.01$ . The real part of the image (shown as an isosurface) corresponds to the reconstructed Bragg electron density, while the complex part of the image,  $\phi$ , is proportional to the displacement field projection. Three states from the reconstructed time sequence are shown.

tice displacement to the true solution. Figure 6b shows that the same conclusion holds for  $t = 42$  minutes. See Figure ?? in the Supplemental Material for central cross-sections that show the amplitude and phase distributions inside the crystal. The average normalized modulus error of the time sequence is improved from 0.2 to 0.1 by including nearest-neighbor information (via  $w = 0.01$ ). Although the reconstructions do not match exactly, the results convey the same overall physical changes in the crystal.

Figure 7 shows that when 3/10 of the required oversampling is used (corresponding to every 5th slice of the original data), major differences in both the reconstructed Bragg electron density and displacement fields arise as compared with the full-rocking-curve reconstructions. There are also disagreements in the reconstructed phases (proportional to the displacements). We therefore conclude that chrono CDI applied to this particular set of measurement data for the chosen time sequence could have decreased the measurement time by a factor of 2 without losing the essential physics of the transforming crystal. For simulated data it could have reduced the time by up to a factor of 20. The discrepancy is likely due to the finite extent in reciprocal space of the real data, noise



in the data, and the unknown support that must be determined via the shrinkwrap algorithm during the reconstruction.

#### IV. DISCUSSION

In this work, we have shown that our new algorithm improves the time resolution of BCDI by a factor of 2 for experimental data and 20 for simulated data. The algorithm thereby enables BCDI investigations of dynamic structural processes in crystals that were previously out of reach and limiting radiation dose in sensitive samples. The time resolution improvements we demonstrate are achieved by reducing the number of 2D measurements made during a 3D Bragg rocking curve, leading to datasets with less than the required oversampling in  $q_z$  at each intermediate time step. The rocking curves across the entire time series are reconstructed simultaneously, enforcing a degree of real-space correlation between solutions at neighboring time steps to account for the reduced oversampling of each individual measurement. The algorithm and its variations should be useful for improving the time reso-

lution of other imaging techniques such as ptychography and tomography<sup>23–27</sup> where there is a continuous relationship in real space between nearest neighbor time states.

#### ACKNOWLEDGMENTS

This material was based upon work supported by the U.S. Department of Energy, Office of Science, under Contract No. DE-AC02-06CH11357. This research used resources of the Advanced Photon Source, which is a DOE Office of Science User Facility. Work at the Advanced Photon Source was supported by the Office of Basic Energy Sciences (BES). P. H. F., S. O. H., and G. B. S. were supported by Basic Energy Sciences, Division of Materials Sciences and Engineering. A. T. and S. M. W. were supported by the Office of Advanced Scientific Computing Research and the ROMPR project. A. U. was supported by an Argonne Director’s postdoctoral fellowship.

The authors thank Jesse N. Clark for insightful discussions.

- 
- <sup>1</sup> M. A. Pfeifer, G. J. Williams, I. A. Vartanyants, R. Harder, and I. K. Robinson, *Nature* **442**, 63 (2006).
  - <sup>2</sup> I. Robinson and R. Harder, *Nature Materials* **8**, 291 (2009).
  - <sup>3</sup> A. Ulvestad, A. Singer, J. N. Clark, H. M. Cho, J. W. Kim, R. Harder, J. Maser, Y. S. Meng, and O. G. Shpyrko, *Science* **348**, 1344 (2015).
  - <sup>4</sup> J. N. Clark, J. Ihli, A. S. Schenk, Y.-y. Kim, A. N. Kulak, M. Campbell, G. Nisbit, F. C. Meldrum, and I. K. Robinson, *Nature Materials* **14**, 780 (2015).
  - <sup>5</sup> A. Ulvestad, A. Singer, H.-M. Cho, J. N. Clark, R. Harder, J. Maser, Y. S. Meng, and O. G. Shpyrko, *Nano Letters* **14**, 5123 (2014).
  - <sup>6</sup> A. Ulvestad, J. N. Clark, A. Singer, D. Vine, H. M. Cho, R. Harder, Y. S. Meng, and O. G. Shpyrko, *Physical Chemistry Chemical Physics* **17**, 10551 (2015).
  - <sup>7</sup> W. Cha, N. C. Jeong, S. Song, H.-j. Park, T. C. Thanh Pham, R. Harder, B. Lim, G. Xiong, D. Ahn, I. McNulty, J. Kim, K. B. Yoon, I. K. Robinson, and H. Kim, *Nature Materials* **12**, 729 (2013).
  - <sup>8</sup> M. Watari, R. A. McKendry, M. Vögli, G. Aeppli, Y.-A. Soh, X. Shi, G. Xiong, X. Huang, R. Harder, and I. K. Robinson, *Nature Materials* **10**, 862 (2011).
  - <sup>9</sup> A. Ulvestad, J. N. Clark, R. Harder, I. K. Robinson, and O. G. Shpyrko, *Nano Letters* **15**, 40664070 (2015).
  - <sup>10</sup> X. Huang, W. Yang, R. Harder, Y. Sun, M. Lu, Y. S. Chu, I. K. Robinson, and H. Kwang Mao, *Nano Letters* **15**, 7644 (2015).
  - <sup>11</sup> G. Xiong, J. N. Clark, C. Nicklin, J. Rawle, and I. K. Robinson, *Scientific Reports* **4**, 6765 (2014).
  - <sup>12</sup> J. N. Clark, L. Beitra, G. Xiong, A. Higginbotham, D. M. Fritz, H. T. Lemke, D. Zhu, M. Chollet, G. J. Williams, M. Messerschmidt, B. Abbey, R. J. Harder, A. M. Korsunsky, J. S. Wark, and I. K. Robinson, *Science* **341**, 56 (2013).
  - <sup>13</sup> A. Ulvestad, M. J. Welland, S. S. E. Collins, R. Harder, E. Maxey, J. Wingert, A. Singer, S. Hy, P. Mulvaney, P. Zapol, and O. G. Shpyrko, *Nature Communications* **6**, 10092 (2015).
  - <sup>14</sup> H. N. Chapman, A. Barty, and S. Marchesini, *Journal of the Optical Society of America A* **23**, 1179 (2006).
  - <sup>15</sup> M. C. Newton, S. J. Leake, R. Harder, and I. K. Robinson, *Nature Materials* **9**, 120 (2010).
  - <sup>16</sup> E. Wicke and H. Brodowsky, *Hydrogen in palladium and palladium alloys*, Vol. 21 (1996) pp. 461–464.
  - <sup>17</sup> T. B. Flanagan and W. A. Oates, *Annual Review of Materials Science* **21**, 269 (1991).
  - <sup>18</sup> S. Marchesini, *Review of Scientific Instruments* **78**, 011301 (2007).
  - <sup>19</sup> A. Tripathi, S. Leyffer, T. Munson, and S. M. Wild, *Procedia Computer Science* **51**, 815 (2015).
  - <sup>20</sup> F. Livet, *Acta Crystallographica Section A: Foundations of Crystallography* **63**, 87 (2007).
  - <sup>21</sup> J. R. Fienup, C. C. Wackerman, and A. Arbor, *Journal of the Optical Society of America A* **3**, 1897 (1986).
  - <sup>22</sup> S. Marchesini, H. He, H. N. Chapman, S. P. Hau-Riege, A. Noy, M. R. Howells, U. Weierstall, and J. C. H. Spence, *Physical Review B* **68**, 140101 (2003).
  - <sup>23</sup> K. Mohan, S. Venkatakrishnan, J. Gibbs, E. Gulsoy, X. Xiao, M. De Graef, P. Voorhees, and C. Bouman, *IEEE Transactions on Computational Imaging* **9403**, 1 (2015).
  - <sup>24</sup> J. W. Gibbs, K. A. Mohan, E. B. Gulsoy, A. J. Shahani, X. Xiao, C. A. Bouman, M. De Graef, and P. W. Voorhees, *Scientific Reports* **5**, 11824 (2015).
  - <sup>25</sup> J. Bø Fløystad, E. T. B. Skjønsvell, M. Guizar-Sicairos, K. Høydalsvik, J. He, J. W. Andreasen, Z. Zhang, and D. W. Breiby, *Advanced Engineering Materials* **17**, 545 (2015).
  - <sup>26</sup> S. O. Hruszkewycz, M. J. Highland, M. V. Holt, D. Kim, C. M. Folkman, C. Thompson, A. Tripathi, G. B. Stephenson, S. Hong, and P. H. Fuoss, *Physical Review Letters* **110**, 177601 (2013).
  - <sup>27</sup> A. Tripathi, J. Mohanty, S. H. Dietze, O. G. Shpyrko, E. Shipton, E. E. Fullerton, S. S. Kim, and I. McNulty, *Proceedings of the National Academy of Sciences of the United States of America* **108**, 13393 (2011).